

NEUTRINO-DRIVEN WINDS IN THE AFTERMATH OF A NEUTRON STAR MERGER: NUCLEOSYNTHESIS AND ELECTROMAGNETIC TRANSIENTS

D. MARTIN, A. PEREGO, AND A. ARCONES

Institut für Kernphysik, Technische Universität Darmstadt, Schlossgartenstr. 2, Darmstadt D-64289, Germany
GSI Helmholtzzentrum für Schwerionenforschung GmbH, Planckstr. 1, Darmstadt D-64291, Germany

F.-K. THIELEMANN

Department of Physics, University of Basel, Klingelbergstraße 82, 4056, Basel, Switzerland

O. KOROBKIN AND S. ROSSWOG

The Oskar Klein Centre, Department of Astronomy, AlbaNova, Stockholm University, SE-106 91 Stockholm, Sweden

(Dated: today)

Draft version September 25, 2015

ABSTRACT

We present a comprehensive nucleosynthesis study of the neutrino-driven wind in the aftermath of a binary neutron star merger. Our focus is the initial remnant phase when a massive central neutron star is present. Using tracers from a recent hydrodynamical simulation, we determine total masses and integrated abundances to characterize the composition of unbound matter. We find that the nucleosynthetic yields depend sensitively on both the life time of the massive neutron star and the polar angle. Matter in excess of up to $9 \cdot 10^{-3} M_{\odot}$ becomes unbound until ~ 200 ms. Due to electron fractions of $Y_e \approx 0.2 - 0.4$ mainly nuclei with mass numbers $A < 130$ are synthesized, complementing the yields from the earlier dynamic ejecta. Mixing scenarios with these two types of ejecta can explain the abundance pattern in r-process enriched metal-poor stars. Additionally, we calculate heating rates for the decay of the freshly produced radioactive isotopes. The resulting light curve peaks in the blue band after about 4 h. Furthermore, high opacities due to heavy r-process nuclei in the dynamic ejecta lead to a second peak in the infrared after 3 – 4 d.

Subject headings: accretion, accretion disks — nuclear reactions, nucleosynthesis, abundances — neutrinos — stars: neutron

1. INTRODUCTION

Since the first detection of neutron star binary systems, the merger of two neutron stars or a neutron star with a black hole has been recognized as an ideal environment for rapid neutron capture (r-process) nucleosynthesis (Lattimer & Schramm 1974, 1976; Eichler et al. 1989). In the r-process, the neutron density is so high that neutrons are captured much faster than the involved nuclei can decay. Once the neutron supply becomes insufficient, the temporarily formed, extremely neutron-rich nuclei decay toward the valley of beta-stability. Approximately half of all the elements heavier than iron are produced in this way.

Matter that is ejected by hydrodynamical interaction and gravitational torques, often referred to as dynamic ejecta, has long been recognized as the likely source of the *heaviest* r-process nuclei (Freiburghaus et al. 1999b; Rosswog et al. 1999; Roberts et al. 2011; Goriely et al. 2011; Korobkin et al. 2012; Bauswein et al. 2013; Hotokezaka et al. 2013; Rosswog 2013; Rosswog et al. 2014). For given nuclear physics input, this type of ejecta yields a very robust, “strong r-process” (Snedden et al. 2008; Goriely et al. 2011; Korobkin et al. 2012; Petermann et al. 2012; Bauswein et al. 2013; Wanajo et al. 2014; Goriely 2015; Just et al. 2015a). This means that all merger

events produce practically identical abundance patterns (for this type of ejecta), independent of the details of the merging system. The abundance pattern, however, shows some sensitivity to the resulting distribution of fission fragments and to the resulting beta-decay half lives (Goriely et al. 2013; Eichler et al. 2015; Goriely 2015).

With increasing sophistication of the included physics and of the numerical techniques also our view on the merger process and its mass loss channels has sharpened. For example, the dynamic ejecta have been recognized to consist of a cold “tidal component” that is launched via gravitational torques and a hotter “interaction component” that comes from the hydrodynamical interaction of the neutron stars (Oechslin et al. 2007; Korobkin et al. 2012). Recent general relativity (GR) simulations of the dynamic ejecta including neutrino transport (Sekiguchi et al. 2015; Foucart et al. 2015) show that shocks in the interaction component significantly increase the temperature. This hotter environment enhances the weak reaction rates. In particular, the larger positron capture and electron neutrino absorption rates on neutrons increase the electron fraction, potentially up to values of 0.4. Therefore, the nucleosynthesis based on these general relativistic simulations can produce the full r-process from the first peak ($A = 80$) to the third one ($A = 195$), see also Goriely et al. (2015). In contrast, Newtonian simulations or approximate GR simulations without weak reactions Goriely et al. (2011); Bauswein

et al. (2013) only produce the heavy r-process elements ($A \geq 130$).

In addition to the dynamic ejecta, the presence of two more mass loss channels has been appreciated and begun to be explored in more detail. These are neutrino-driven winds (Ruffert et al. 1997; Rosswog & Ramirez-Ruiz 2002; Dessart et al. 2009; Perego et al. 2014; Just et al. 2015a) and late-time accretion disk disintegration (Metzger et al. 2008; Beloborodov 2008; Lee et al. 2009; Fernández & Metzger 2013; Just et al. 2015a). The late-time disintegration of the accretion disk, driven by viscous heating and recombination of free nucleons into alpha particles, is referred to as viscous ejecta in the following.

The historically favored production site, core-collapse supernovae, in contrast, seems to struggle to produce the conditions required for a successful r-process (Arcones et al. 2007; Hudepohl et al. 2010; Roberts et al. 2010; Fischer et al. 2010; Arcones & Montes 2011; Arcones & Thielemann 2013), though some rare supernovae may plausibly contribute (Fujimoto et al. 2006, 2008; Winteler et al. 2012; Mösta et al. 2014; Nishimura et al. 2015).

The idea that compact binary mergers could be the sources of the heaviest r-process elements has recently received strong support from an observed near-infrared transient in the aftermath of a short gamma-ray burst (sGRB) (Tanvir et al. 2013; Berger et al. 2013; Yang et al. 2015). This emission has been interpreted as being a “kilonova” (Metzger et al. 2010) (sometimes referred to as “macronova”, cf. Kulkarni (2005)), a transient that is powered by the radioactive decay of freshly synthesized r-process elements. In particular the luminosity peak after only several days and in the near-infrared – rather than after hours in the optical/UV as originally expected (Li & Paczyński 1998) – supports the view that the ejecta are made of very heavy r-process elements that result in effective opacities that are orders of magnitude larger than those of supernovae (Kasen et al. 2013; Barnes & Kasen 2013; Tanaka & Hotokezaka 2013; Grossman et al. 2014). If this interpretation is correct, this would for the first time link compact binary mergers with GRBs observationally, a long suspected, but actually so far unproven connection, and also with the formation of very heavy elements. Such kilonovae are an important facet in the multi-messenger view of compact binary mergers (Rosswog 2015) and, since they emit quasi-isotropically, they may become crucial in assuring the first direct gravitational wave detections (Metzger & Berger 2012; Nissanke et al. 2013; Piran et al. 2013).

Despite all of these promises, the role of compact binary mergers for the chemical enrichment histories of galaxies, in particular at early times, is not yet sufficiently well understood. While earlier work (Argast et al. 2004) disfavored them as dominant source of r-process in the early galaxy, more recent studies are either more optimistic about their role (Matteucci et al. 2014) or actually favor them over supernovae as major production site, see for example the recent hydrodynamical studies of Shen et al. (2015) and van de Voort et al. (2015). Here more work is clearly indicated to settle the case (see Cescutti et al. (2015); Wehmeyer et al. (2015)).

Understanding the different mass loss channels, their nucleosynthesis and possible electromagnetic transients is of prime importance for cosmic nucleosynthesis and

galactical chemical evolution, for gravitational wave detection strategies and actually also for the GRB launch mechanism, since already a tiny mass loading of a fireball can “choke” an emerging jet (Murguia-Berthier et al. 2014). In this paper, we focus on the neutrino-driven wind from a post-merger remnant that consists of a central massive neutron star (MNS) surrounded by an accretion disk and present a comprehensive nucleosynthesis study based on the first three dimensional simulation recently performed by Perego et al. (2014). In the latter work preliminary nucleosynthesis results based on ten representative trajectories were presented. Here, we follow the nucleosynthetic evolution based on 17 000 trajectories and we discuss the implications for radioactively powered electromagnetic transients.

The paper is structured in the following way. In Sect. 2 we briefly describe the hydrodynamical simulations, the tracers used to follow the ejecta and the physical input of the reaction network. We present the results of the nucleosynthesis calculations and report on time and angle dependency of the neutrino-driven wind in Sect. 3. Furthermore, we consider mixing with the other channels of matter ejection and calculate the electromagnetic signal. Finally, we discuss our results and their implications in Sect. 4.

2. METHODS

2.1. Hydrodynamical simulations

Our nucleosynthesis study is based on the first three dimensional, Newtonian simulation of the neutrino-driven wind that emerges during the aftermath of a binary neutron star merger (Perego et al. 2014). The merger remnant is characterized by a long-lived massive neutron star, surrounded by a quasi-Keplerian accretion disk with an initial mass of $M_{\text{disk}} \simeq 0.19M_{\odot}$. For the present analysis, we repeat and extend the previous simulation to longer times, and we follow a substantially larger number of particles.

We use the parallel grid code FISH (Käppeli et al. 2011) to solve the hydrodynamical equations on a uniform Cartesian grid. Nuclear matter description is provided by the TM1 nuclear equation of state, supplemented with electron-positron and photon contributions (Timmes & Swesty 2000; Hempel et al. 2012). As initial condition we use a late matter configuration from a three dimensional high resolution simulation of two non-spinning $1.4 M_{\odot}$ neutron stars (e.g. Price & Rosswog (2006)). Neutrino-matter interactions are taken into account using the multiflavor Advanced Spectral Leakage (ASL) scheme, see Perego et al. (2015, in preparation). It models the neutrino emission effectively by smoothly interpolating between diffusive and free-streaming rates, separately for different neutrino energies, and it has been carefully gauged at full transport calculations. Neutrino absorption is also included in optically thin conditions, based on the calculation of the neutrino densities outside the neutrino last scattering surfaces. The list of the neutrino reactions implemented inside the ASL scheme can be found in table 1 of Perego et al. (2014). The present simulation corresponds to an extension of the one presented in Perego et al. (2014). The simulations starts at 25 ms after the beginning of the merger, including 10 ms of relaxation of the SPH final conditions

on the grid, and follows the post merger evolution for 190 ms. The temporal evolution of the neutrino luminosities and mean energies during the whole simulation follows the same trends reported in Fig. 10 of Perego et al. (2014) for the first 90 ms. The relevant mean energies stay approximately constant: ~ 11 MeV for the electron neutrinos and ~ 15.5 MeV for the electron antineutrinos. The total neutrino luminosities, integrated over the whole solid angle, decrease slowly with time. At the end of the simulation ($t_{\text{sim}} \approx 190$ ms) the electron (anti)neutrino luminosity due to cooling processes only is equal to $\sim 2.2 \cdot 10^{52}$ erg/s ($\sim 2.9 \cdot 10^{52}$ erg/s), while the inclusion of the neutrino absorption in optically thin conditions decreases it to $\sim 1.5 \cdot 10^{52}$ erg/s ($\sim 2.4 \cdot 10^{52}$ erg/s). Due to the larger optical depth along the equatorial plane, the neutrino fluxes measured far from the MNS along the polar direction are roughly 3 times larger than the ones in the equatorial plane (cf. Fig. 12 of Perego et al. (2014)).

The inclusion of the energy deposition provided by the neutrino absorption on nucleons inside the disk drives a baryonic wind on a time scale of tens of milliseconds, see Fig. 1. Matter expanding inside the wind becomes unbound at a distance $\lesssim 600$ km from the center. The resulting ejecta are confined within a polar angle of 60° , measured from the rotational axis of the disk. Due to the strong neutrino irradiation, the initially highly neutron rich matter inside the disk changes its electron fraction in the wind. The dominant ν_e -absorption of neutrons raises Y_e toward equilibrium values (see e.g. Qian & Woosley (1996)). The evolution towards this equilibrium value may be affected by general relativistic treatment of the merger phase. GR simulations of a binary neutron star merger including neutrinos (Neilsen et al. 2014) and following the onset of the neutrino-driven wind (Sekiguchi et al. 2015) indicate that the luminosities can be larger than in Newtonian simulations, due to the higher temperature inside the massive neutron star and the disk. However, the ratio between the electron neutrino and antineutrino luminosities is similar in both cases, as well as the values of the mean energies. Therefore, the equilibrium electron fraction is expected to be almost the same, while the evolution towards this Y_e should be faster in the GR simulations. This difference does not come directly from the Newtonian treatment of the disk and of the wind, but from the initial profiles resulting from the merger process.

2.2. Tracers from the hydrodynamical simulation

At the beginning of our simulation we place 10^5 tracers inside our computational domain. The wind tracers are ejected from a region with initial density of $\rho \lesssim 10^{10} \text{ g cm}^{-3}$, as found in backtracking procedures of preliminary tests following Perego et al. (2014). Thus, we locate our tracers initially inside the thick accretion disk where the density is between $2 \cdot 10^6 \text{ g cm}^{-3}$ and $2 \cdot 10^{10} \text{ g cm}^{-3}$ (see Fig. 2). The number of tracers assigned to each grid cell is proportional to its mass content and the actual location of each particle within a cell is randomly assigned. Hence, the resulting tracer distribution tracks the matter density distribution inside the disk. The mass of the region of the disk where the tracers are placed is $0.0542 M_\odot$. Therefore, we assign to each

of them an inherent mass of $m_i = m = 5.420 \cdot 10^{-7} M_\odot$. Every tracer records the local properties of matter (density, internal energy, electron fraction and velocity components) at its present location by linearly interpolating the corresponding values on the computational grid. The total specific energy, e_{tot} , is computed as the algebraic sum of the kinetic, thermal and gravitational specific energy. We recall here that the thermal energy is obtained from the relativistic internal energy, reduced by the rest mass energy (both obtained from the nuclear equation of state). All tracers are passively advected by the fluid and their location is evolved in time inside the grid by solving the equation $d\vec{x}/dt = \vec{v}$ with a second order accurate Euler integration scheme. A tracer particle is considered unbound if $e_{\text{tot}} > 0$ and if its radial component of the velocity is positive, steadily from a certain time until the end of the simulation. For each ejected tracer, neutrino fluxes and mean energies as a function of time come from the axisymmetric output provided by the hydrodynamic simulations, see Sect. 2.1 and Perego et al. (2014).

2.3. Nucleosynthesis network

For the post-processing of the tracers, a complete nucleosynthesis network (Winteler 2012; Winteler et al. 2012) is employed. Over 5800 nuclei between the valley of stability and the neutron drip line are considered, i.e. isotopes from H to Rg. The reaction rates are taken from the compilation of Rauscher & Thielemann (2000) for the Finite Range Droplet Model (FRDM, Möller et al. (1995)). Weak interaction rates including neutrino absorption on nucleons are taken into account (Möller et al. 2003; Fröhlich et al. 2006). Furthermore, neutron capture for nuclei with $Z \gtrsim 80$ and neutron-induced fission rates are given by Panov et al. (2010) as well as β -delayed fission probabilities from Panov et al. (2005).

We perform nucleosynthesis calculations for over 17 000 ejected tracers from the hydrodynamical simulation (see Sect. 2.2). Our computations start when the temperature drops below $T = 10$ GK. Then the initial composition is determined by nuclear statistical equilibrium (NSE) and is dominated by alpha particles, neutrons, and protons. NSE is assumed to hold for $T \gtrsim 8$ GK. Between $10 \text{ GK} > T > 8 \text{ GK}$, the network evolves the weak reactions since they are not in equilibrium and change the Y_e accordingly. As soon as the temperature undershoots the NSE threshold, the full network provides the abundances. The longest trajectories were simulated until $t_{\text{sim}} \sim 200$ ms, therefore we extrapolate them following the prescription outlined in Korobkin et al. (2012).

Moreover, the energy generation by the r-process is calculated and its impact on the entropy is included (Freiburghaus et al. 1999b). As is common practice, we neglect the feedback of nuclear heating on the density evolution. In the case of the dynamic ejecta, it has been shown that this approximation is very good for nucleosynthesis calculations, although the long-term hydrodynamical evolution of the ejecta is heavily influenced¹ (Rosswog et al. 2014). The heating mainly originates from β -decays and we assume that the energy is

¹ We expect that the impact on the nucleosynthesis in neutrino-driven winds is small, but since the expansion time scales here are different from the dynamic ejecta, this issue may need further scrutiny in the future.

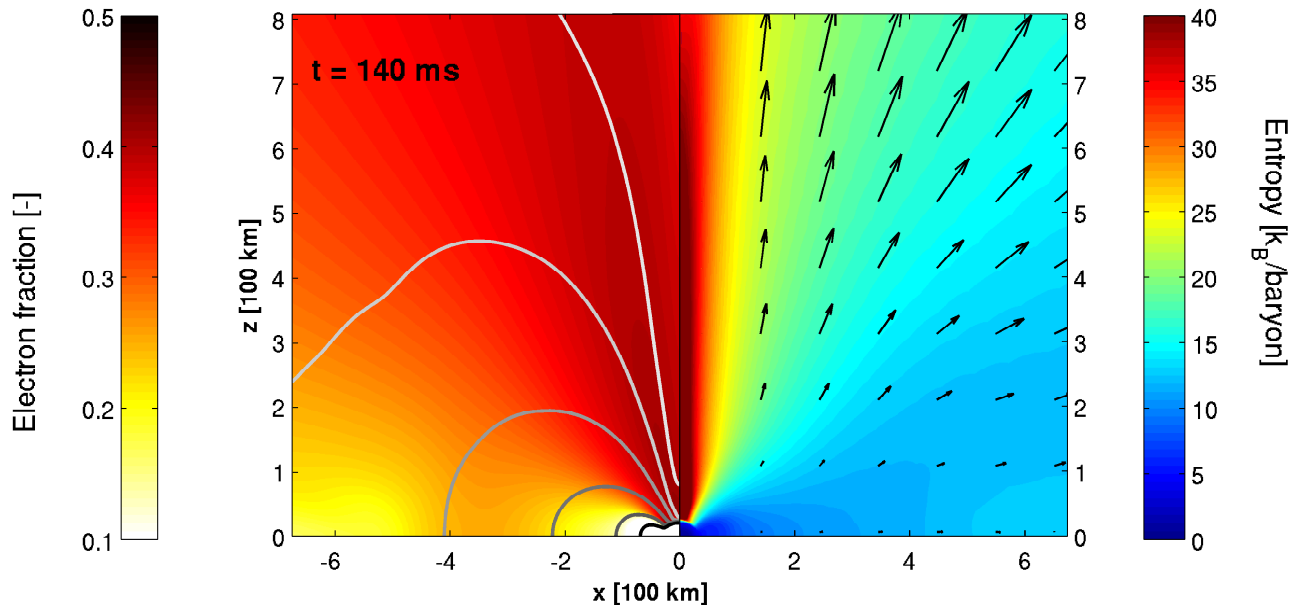


FIG. 1.— $x - z$ plane at 140 ms after the beginning of the simulation. The left panel shows the electron fraction with a superimposed contour plot of the density. A color gradient from white to black indicates the regions with densities of $\rho = 10^6 \text{ g/cm}^3$ to $\rho = 10^{11} \text{ g/cm}^3$. Entropy profile and the projected velocity are presented in the right panel. The length of the arrows characterizes the magnitude of the velocity.

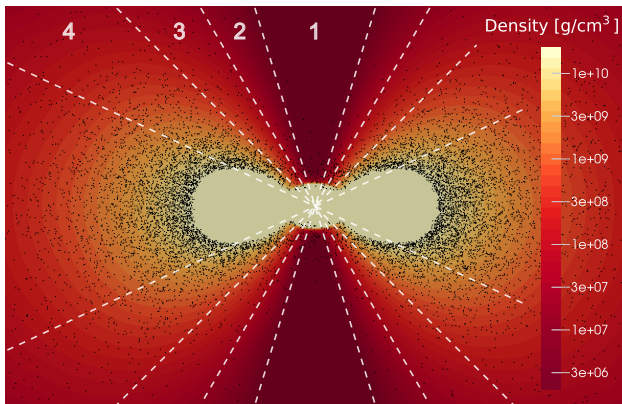


FIG. 2.— Distribution of the tracers in the $x - z$ plane at the beginning of the simulation. The density profile is shown for $2 \cdot 10^6 \text{ g cm}^{-3} \leq \rho \leq 2 \cdot 10^{10} \text{ g cm}^{-3}$. Tracers are marked by black dots, white dashed lines and numbers label the four angular regions of interest, which are referred to as (angular) bins 1 – 4 in the following.

roughly equally distributed between thermalizing electrons and photons, and escaping neutrinos and photons (Metzger et al. 2010).

3. NUCLEOSYNTHESIS

3.1. Time and angle dependency

The composition and amount of matter ejected in the neutrino-driven wind depends on the temporal evolution of the disk and the fate of the compact central object. Here we consider a long-lived MNS. In the following, we present abundances at various times after the merger and for different latitudes to understand the angular distribution and temporal evolution of ejected matter. The potential consequences for the mixing with the dynamic ejecta and thus for the light curve are discussed in Sects. 3.2 and 3.3, respectively. In the following, t_{sim} ,

refers to the time since merger. When abundances are shown at t_{sim} , we consider all tracers having become unbound until this time. Therefore, at later times early ejecta are also included.

An idea of the amount of matter ejected and its potential composition can be gained by exploring the dependence of the ejected mass on the electron fraction and time. This evolution is shown in Fig. 3. Within the first 50 ms only a marginal amount of mass with electron fraction $Y_e \lesssim 0.3$ gets unbound. Until $t_{\text{sim}} = 100$ ms approximately $2 \cdot 10^{-3} M_\odot$ are ejected with a central value of $Y_e \approx 0.3$. After almost twice that time, i.e. $t_{\text{sim}} = 190$ ms, the mass of unbound material reaches $9 \cdot 10^{-3} M_\odot$. These late-time ejecta has relatively high electron fractions (with a mean value between 0.3 and 0.35) since neutrinos have more time to interact with nucleons. Furthermore, the growth rate of unbound mass by the late ejection of tracers remains approximately constant from 110 ms on. The substantial mass accretion rate inside the accretion disk, amounting to a few tenths of solar masses per second, provides quasi steady-state conditions with neutrinos as primary cooling agent. As a consequence, the neutrino luminosities decrease only slowly over the expansion time scale (cf. Fig. 10 in Perego et al. (2014)) and the interaction rates get close to equilibrium.

In the following, abundances are shown using either of these two normalizations for a given nuclear mass A :

- Total mass:

$$X_{\text{tot}}(A) = \sum_{i=1}^N X_i(A) \cdot m_i, \quad (1)$$

with N , X_i and m_i being the number of tracers considered, the mass fractions and the mass of one tracer i , respectively. This quantity has mass units

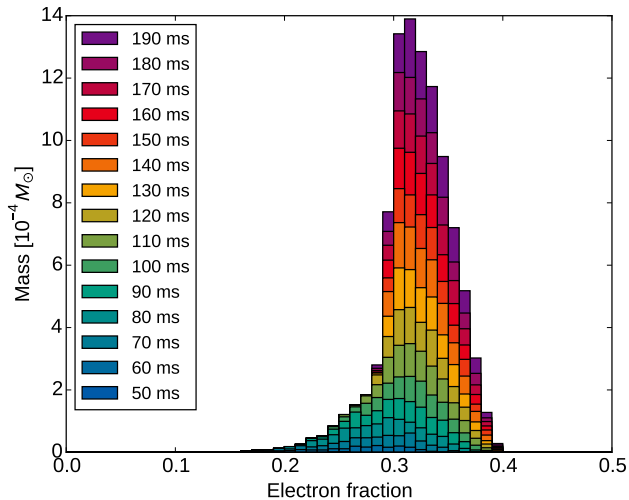


FIG. 3.— Evolution of the electron fraction for ejected tracers. The Y_e distributions at various simulation times are represented by superposing bars with different colors.

and thus allows to compare different ejection channels to each other, as we will discuss in Sect. 3.2.

- Integrated abundances:

$$Y_{\text{int}}(A) = \frac{\sum_{i=1}^N Y_i(A) \cdot m_i}{\sum_{i=1}^N m_i}. \quad (2)$$

Normalizing the abundances via Eq. (2) allows to explore the average nucleosynthesis yields of a certain subclass of tracers, for instance tracers ejected into a particular solid angle. Additionally, the impact of single trajectories on the overall nucleosynthesis is directly evident from the comparison with the average abundance curve.

Figure 4 shows total ejected masses for simulation times $t_{\text{sim}} = 90$ ms, 140 ms and 190 ms. The heavy nuclei beyond the second r-process peak ($A \sim 130$) are produced by early, very neutron-rich ejecta, as indicated by the overlap of the three curves at different simulation times. Later on, no heavy r-process elements ($A \gtrsim 130$) are produced any more. There is a threshold $Y_e \sim 0.25$ below which heavy r-process elements (i.e., beyond the second peak at $A = 130$) can be synthesized (see also Kasen et al. (2015)). As time passes, a substantial amount of tracers contributing to nuclei with $A \lesssim 120$ becomes unbound. This evolution is in fact a direct consequence of the trend of Y_e presented in Fig. 3.

In addition, the nucleosynthesis has an angular dependency. We divide the neutrino-driven wind into four regions above and below the disk by setting cuts on the polar angle and investigate the angular dependence of the ejecta. Each of the cuts has a width of $\Delta\theta = 15^\circ$, hence the whole neutrino-driven wind is captured within $0^\circ \leq \theta \leq 60^\circ$ (as a convention we define $\theta = 0^\circ$ at the poles). These four regions or bins are indicated in Fig. 2 with white dashed lines and are labeled with the number of the bin. The properties of the tracers ejected until $t_{\text{sim}} = 190$ ms in each of the angular bins are shown in Figs. 5 and 6, when passing a sphere with a radius of 750 km. We select the nucleosynthesis-relevant quantities: electron fraction Y_e , entropy per baryon s and radial

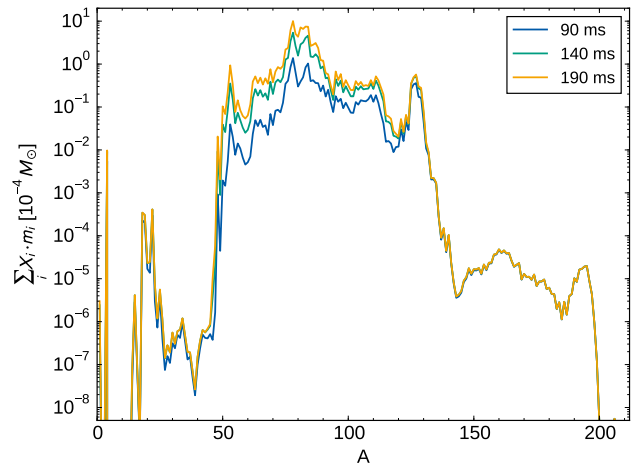


FIG. 4.— Total final mass fractions times the mass of the ejecta until $t_{\text{sim}} = 90$ ms, 140 ms and 190 ms. Early neutron-rich ejecta produce heavy r-nuclei with $A \gtrsim 130$, leading to overlapping abundances in this region. Later ejecta contribute strongly to the lighter heavy elements (note the logarithmic ordinate).

velocity v_r . The major part of the cumulative mass is approximately equally distributed to the two angular bins close to the accretion disk. On the contrary, the two bins in the polar region contain 15% – 20% of the total cumulative mass. While the entropy of the unbound tracers ranges from $10 k_B/\text{baryon}$ to $30 k_B/\text{baryon}$ (Fig. 5), it is still very low and has therefore little impact on the nucleosynthesis. The radial velocity provides a measure for the dynamical time-scale and is constrained to $0.04c - 0.08c$ (Fig. 6). In the neutrino-driven wind the nucleosynthesis is most sensitive to the electron fraction distribution which varies for every angular region. As a general trend, the average electron fraction decreases as a function of the angle and reaches values down to 0.3 for the two zones closest to the disk. Both of these bins also contain extreme cases with very neutron-rich conditions of $Y_e < 0.2$.

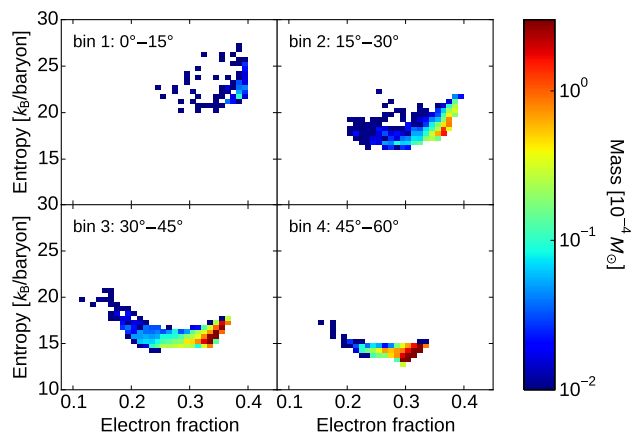


FIG. 5.— Distribution of the unbound tracers in the $Y_e - s$ plane at a sphere with a radius of 750 km. We present the logarithmic scale of the total mass for all tracers in a certain angular bin of the $Y_e - s$ plane with a color code. The panels correspond to the angle intervals defined in Fig. 1.

Figure 7 shows the resulting integrated abundances for tracers ejected at $t_{\text{sim}} = 140$ ms. All yields are presented

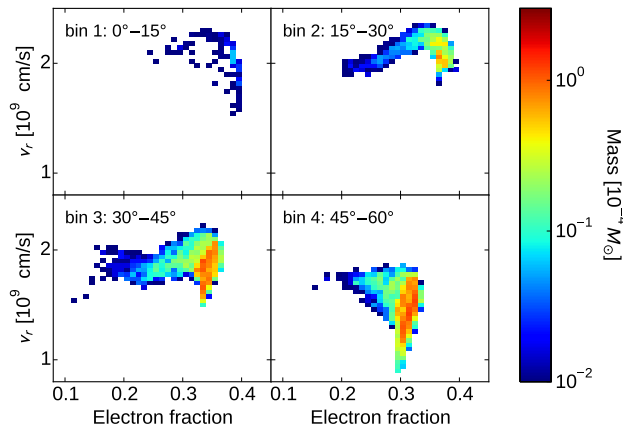


FIG. 6.— Same as Fig. 5, but for the $Y_e - v_r$ plane.

in comparison to the solar abundances (dots, Lodders (2003)) for one angular bin in every panel. The thin gray lines represent individual tracers, while averages are indicated by a solid thick line in every panel. The patterns in Fig. 7 reveal significant differences in abundances for distinct latitudes. We find that the first r-process peak ($A \sim 80$) forms for each angular region, whereas the second abundance peak ($A \sim 130$) is only reached in bin 3 and bin 4. In particular, the angular zone closest to the disk, i.e., bin 4, successfully attains elemental abundances close to the solar system values up to the second abundance peak (bin 1), less heavy elements are synthesized.

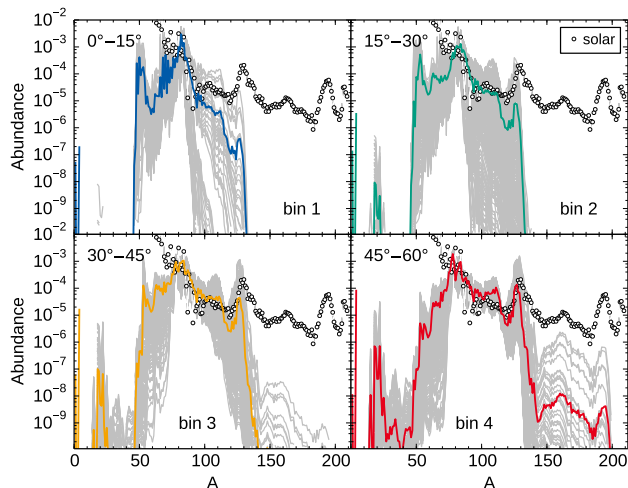


FIG. 7.— Individual abundances and integrated final abundances for ejecta until $t_{\text{sim}} = 140$ ms in each of the four considered angular bins. Thick colored lines mark the average yields for each angular region. Note that we apply the same color code consistently in all following figures. Moreover, thin gray lines denote abundances from individual trajectories to hint the variety of the nucleosynthesis. Solar abundances are shown with dots for comparison.

To gain further insights into the dependence on time, it is instructive to compare the trends of the angular bins at various times. Total masses as a function of mass number A (Eq. (1)) for unbound tracers at $t_{\text{sim}} = 90$ ms, 140 ms and 190 ms are presented in Fig. 8. At early times $t_{\text{sim}} \lesssim 90$ ms, elements up to $A \sim 120$ are produced predominantly by the ejecta in bin 3, while only

bin 4 synthesizes nuclei within the vicinity of the third abundance peak ($A \sim 195$). The yields resulting from both bin 3 and bin 4 clearly dominate the abundances, as is expected from the distribution of the mass and the electron fraction for the tracers among the four bins (cf. Figs. 5 and 6). In contrast, bin 1 and bin 2 give marginal contributions. With time, increasing yields for lighter heavy nuclei ($A \lesssim 120$) (cf. Fig. 4) are present in all considered angular regions.

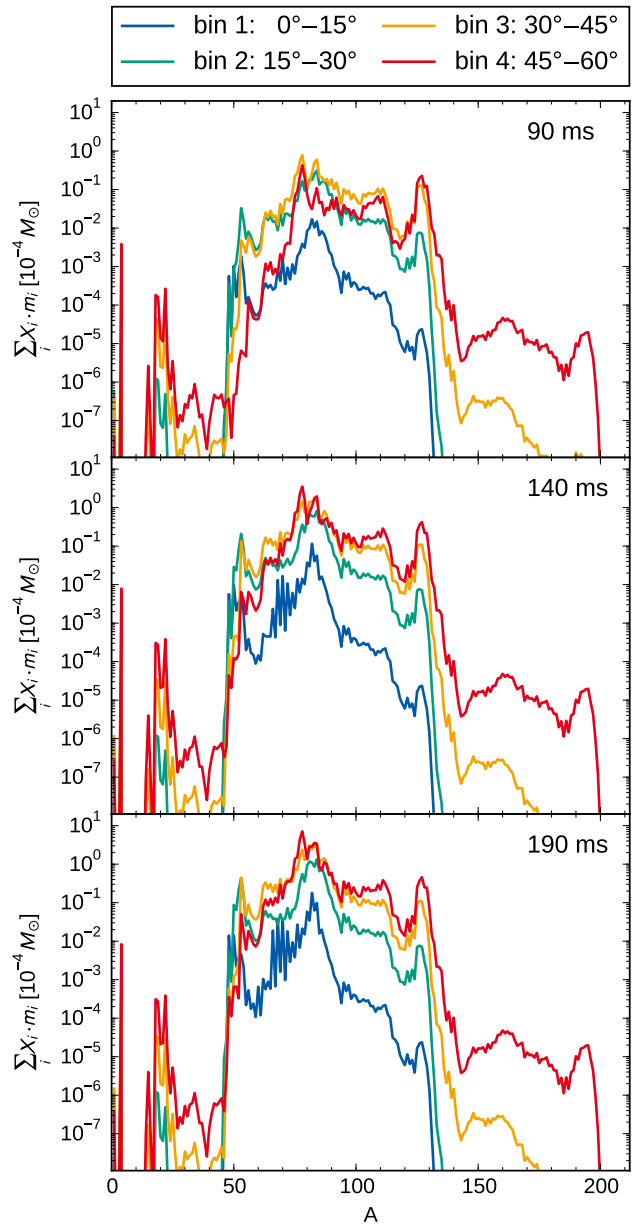


FIG. 8.— Total final masses. The panels show the yields for tracers ejected until $t_{\text{sim}} = 90$ ms, 140 ms and 190 ms from top to bottom. We use the same color scheme as in Fig. 7 to identify the different angular bins.

Let us take a closer look at the relevant physical quantities characterizing the nucleosynthesis. Figure 9 shows the evolution of individual electron fractions for tracers unbound at 140 ms (gray, thin lines), along with the corresponding average curves (colored, thick lines). Note

that the elapsed time of a tracer is defined with respect to the moment when it gets out of NSE in the network calculations. The individual tracers provide information about the spread in the initial Y_e (i.e. at $T = 10$ GK), also visible in Figs. 5 and 6. The slight increase of the electron fraction shortly after the beginning of the calculations is due to neutrino absorption on nucleons, whereas the steep rise at around $t \simeq 10^{-1}$ s is caused by β -decays.

The electron fraction in the neutrino-driven wind depends on the competition between the expansion and the weak equilibrium time scales, on the ratio between the ν_e and $\bar{\nu}_e$ luminosities, as well as on the neutrino mean energies (e.g., Qian & Woosley (1996)). As we mentioned in Sect. 2.1, the larger luminosities predicted by GR simulations can lead to a faster evolution towards the equilibrium Y_e . Therefore, the very small amount of heavy elements ($A > 130$) that are produced in the initial phase of our Newtonian simulation may not be present in a GR simulation. In addition to the GR effects, an accurate calculation of Y_e would require the usage of a detailed neutrino transport scheme, which is presently computationally prohibitive in long-time three dimensional simulations, without global symmetries. Assuming uncertainties of the order of 20% for the neutrino luminosities and of 10% for the mean energies², we estimate a potential uncertainty of $\sim 15\%$ on the values of the equilibrium electron fraction. Given the broad range of Y_e obtained in the ejecta (Figs. 5, 6 and 9), we consider this uncertainty as being important to be mentioned, but not crucial for our analysis.

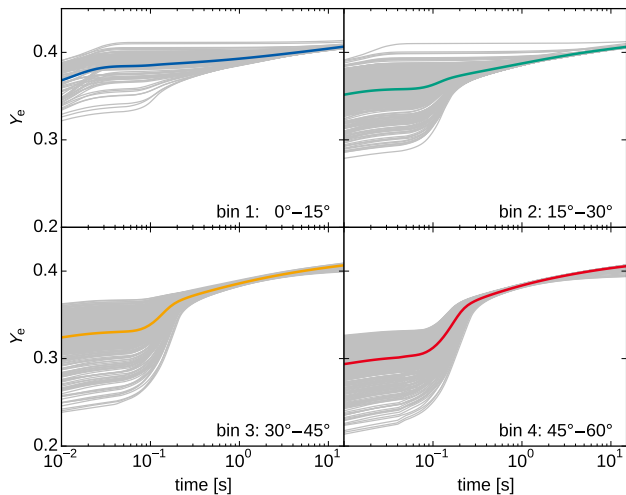


FIG. 9.— Temporal evolution of the electron fraction for tracers that become unbound until $t_{\text{sim}} = 140$ ms. The solid thick lines are averages $\langle Y_e \rangle$ for every angular bin as introduced in Fig. 7. Thin gray lines represent individual tracers.

In order to examine the production of heavy elements, we present the evolution of neutron density n_n , the average mass number $\langle A \rangle$ and the average proton number $\langle Z \rangle$ in Fig. 10 for different angular regions. At the be-

² This estimate is consistent with the quantitative differences spotted between our ASL scheme results and the ones obtained using a multigroup flux limited diffusion transport in axisymmetric simulations (Dessart et al. 2009).

ginning, the neutron density is larger than 10^{30} cm^{-3} and the composition is dominated by alpha particles and neutrons. The onset of the r-process nucleosynthesis is triggered when the temperature decreases to ~ 3 GK (marked by triangles in the top panel of Fig. 10; see, e.g., the dependence of r-process efficiency as a function of entropy, electron fraction and expansion time scale, Hoffman et al. 1997; Freiburghaus et al. 1999a). For $t \simeq (1.5 - 3.0) \cdot 10^{-1}$ s, most of the neutrons are consumed as indicated by the rapid neutron density drop. After this, matter beta-decays to stability and this leads to an increase of Y_e (see Fig. 9). Then, the mass number stagnates, since no more heavy elements are formed (see middle panel of Fig. 10). No fission takes place, resulting in the monotonic evolution of mass and proton number. The higher neutron density in bin 4 favors the build-up of heavier nuclei compared to the other regions. With decreasing polar angle the neutrons are consumed earlier, as their initial density is smaller and the expansion velocity of the corresponding tracers is larger.

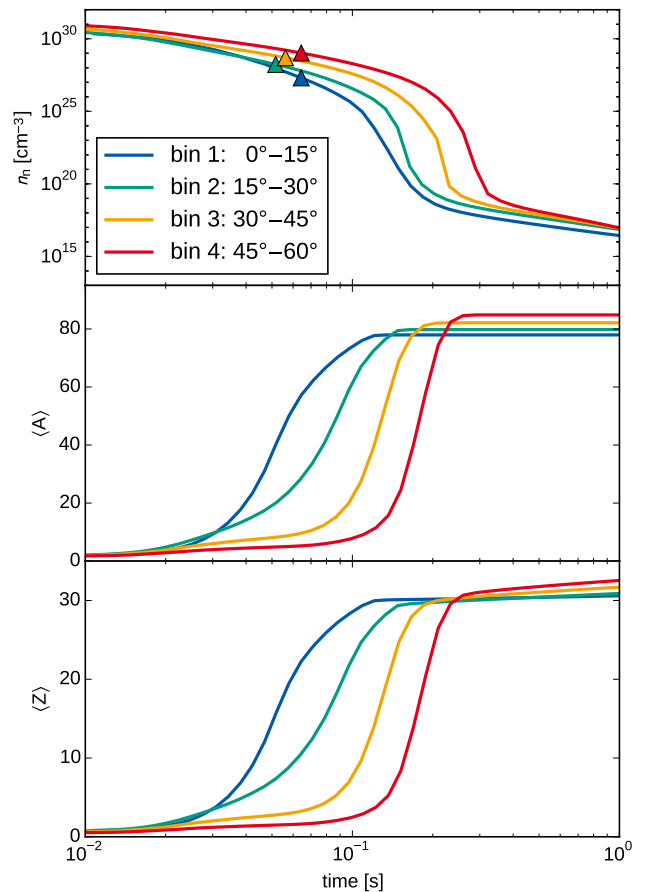


FIG. 10.— Evolution of the neutron density n_n (top), average mass number $\langle A \rangle$ (middle) and average proton number $\langle Z \rangle$ (bottom). The solid lines follow the mean values of the four angular bins (see also Fig. 9). Triangles indicate times, when the temperature reaches $T = 3$ GK, i.e. the onset of the r-process.

3.2. Neutrino-driven wind and dynamic ejecta

The neutrino-driven wind is only one of three nucleosynthesis-relevant ejecta in neutron star mergers.

In order to have the complete nucleosynthesis picture, one would need to follow the evolution of the dynamic and disk (neutrino- and viscous-driven) ejecta, and investigate how they mix. However, this is currently too complicated to be studied in a single simulation due to the different time-scales and physics involved. The dynamic ejecta expand very fast from the beginning. While neutrinos may be initially important for the Y_e their impact is insignificant when the disk becomes transparent (Fernández & Metzger 2013; Metzger & Fernández 2014; Just et al. 2015a). Nevertheless, mixing of the different types of ejecta can occur once the unbound matter becomes considerably decelerated by the ambient medium. Where this happens depends on the merger location with respect to the galaxy. Simple estimates indicate that the time scale for being noticeably decelerated is by far greater than years, see, for example, the discussion in Sect. 2.1 of Rosswog et al. (2014)).

In the first study of the mixing between the disk and dynamic ejecta, Fernández et al. (2015) showed that there is no significant mixing between these ejecta. This study focused on neutron star black hole mergers, where neutrino-driven ejecta are less important as it was discussed also by Fernández & Metzger (2013) compared to Metzger & Fernández (2014). However, their conclusion may also apply to our results that are based on a long-lived MNS. From the nucleosynthesis perspective, Just et al. (2015a) have also investigated the mixing of disk and dynamic ejecta. They have modeled the long-time evolution of a black hole surrounded by a disk where matter is neutrino- and viscous-driven ejected. In a post-processing step, the nucleosynthesis of such simulations was added to the dynamic ejecta from a merger simulation (Bauswein et al. 2013).

We combine the nucleosynthesis of the neutrino-driven wind presented in Sect. 3.1 with the dynamic ejecta computed by Korobkin et al. (2012). Although the ejecta masses show a substantial spread depending on the parameters of the merging binary system (Rosswog 2013), the resulting abundance patterns have been found to be practically identical (Korobkin et al. 2012). In contrast to previous studies (i.e., Fernández & Metzger (2013); Just et al. (2015a)) with a black hole as central object, we assume a long-lived MNS. This has strong consequences on the amount and properties (i.e., Y_e) of the matter ejected by neutrinos as discussed by Perego et al. (2014); Metzger & Fernández (2014); Kasen et al. (2015).

The comparison between dynamic and wind ejecta is given in Fig. 11 showing the total ejected masses (Eq. (1)) as a function of A for both contributions. Note that the approach here differs from the one in the previous sections, in which we treated the different times t_{sim} to be merely snapshots of the neutrino-driven wind. Now, we assume that the MNS collapses after t_{sim} , terminating the ejection of further material in the wind. Three different simulation times are considered, $t_{\text{sim}} = 90$ ms, 140 ms, and 190 ms. This comparison indicates that the wind ejecta complement the dynamic ejecta by producing elements below the second peak. We note that if the dynamic ejecta could produce the full r-process, as suggested by recent GR simulations (Wanajo et al. 2014; Sekiguchi et al. 2015) and by parametric studies (Goriely et al. 2015), the combination of the dynamic and wind nucleosynthesis would again allow the production of

lighter heavy elements ($A < 130$) in addition to the heavy r-process. In the latter case, the wind ejecta would increase only the relative contribution of the lighter heavy elements. Moreover, the amount of wind ejecta becomes comparable to the dynamic ejecta if the MNS survives long enough ($t_{\text{sim}} \gtrsim 140$ ms in our model). These ejecta amounts will be further enhanced by viscous ejecta that can produce r-process elements from the first to the third peak (Just et al. 2015a). If the three ejecta completely mix, the wind contribution may still lead to variations in the abundances below $A = 130$ (i.e., $Z < 50$). Such variations are also expected from observations of the oldest stars (see Sneden et al. (2008) for a review). The size of the observed variations could help to constrain different contributions of the three ejecta types to the r-process abundances.

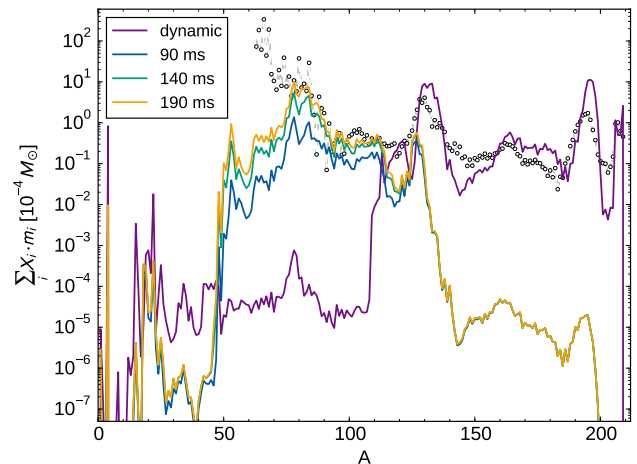


FIG. 11.— Comparison of the nucleosynthesis yields for neutrino-driven wind (cf. Fig. 4) and dynamic ejecta (labeled with dynamic). While the dynamic ejecta produce very heavy nuclei, the neutrino-driven wind complements its abundances by producing the lighter heavy elements from the first to the second r-process peak.

The oldest observed stars were formed in an interstellar medium polluted by only one or few nucleosynthesis events. Therefore, their atmospheres present a unique fingerprint for the r-process. Observations indicate that there are at least two types of abundance patterns among the oldest r-process stars (see, e.g., Sneden et al. (2008); Qian & Wasserburg (2007)): 1) stars with high enhancement of heavy elements ($Z > 50$) present a robust pattern for those and some variations for the lighter heavy elements ($Z < 50$); 2) stars with low enhancement of heavy r-process. Two stars are typically identified with these trends: 1) CS 22829-052 (Sneden et al. 2003) and 2) HD 122563 (Wallerstein et al. 1963; Honda et al. 2004, 2006). Recently, Hansen et al. (2014) have shown that this second kind of pattern can be explained by the superposition of two components: an H-component producing the heavy r-process elements (and maybe also lighter ones) and an L-component contributing only below $Z = 50$. In neutron star mergers, the dynamic and viscous ejecta can account for the H-component while the wind ejecta would be the L-component. Matter with a perfect mixing of the three ejecta will lead to a pattern like in CS 22829-052. This is shown in the upper

panel of Fig. 12, where the combination of wind (L-component) and dynamic (H-component) ejecta reproduce the observed abundances. The differences around the third peak are due to nuclear physics input as shown in e.g. Eichler et al. (2015). If the mixing is not perfect and the wind ejecta combines only with a small amount of dynamic and/or viscous ejecta, then one can explain the trend observed in HD 122563 (see also Just et al. (2015a)). This is shown in the bottom panel of Fig. 12 where the dynamic ejecta has been reduced by a factor of 50. In this case, one would expect to have more variability in the observations depending on the amount of the H-component that is mixed. Indeed observations show variability for $Z > 50$ in these kind of stars (Roederer et al. 2010; Hansen et al. 2014).

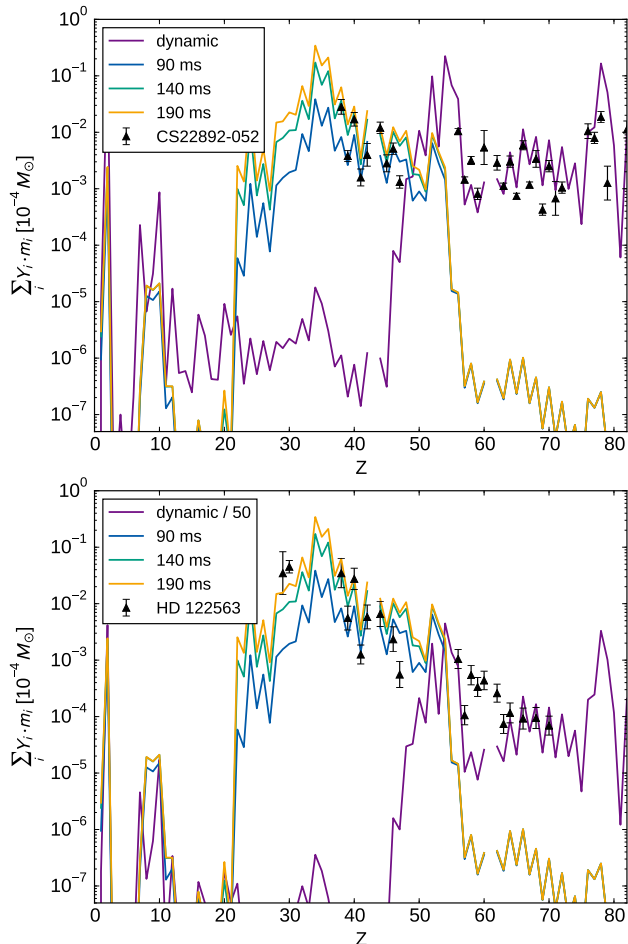


FIG. 12.— Top: combined elemental abundances of neutrino-driven wind and dynamic ejecta in comparison to the yields of the metal-poor star CS22892-052 (Snedden et al. 2003). Abundances are weighted with the ejecta mass to consistently add the two contributions. Bottom: comparison of the combined yields with the ones of the HD stars (Wallerstein et al. 1963; Honda et al. 2004, 2006). Note that the dynamic ejecta are scaled down by a factor of 50.

On the time scale of star formation, it is likely that all the ejecta have efficiently mixed, even if the wind expands perpendicular to the disk and the other two are more homogeneously distributed or stay in the disk plane. Do we expect stars to be polluted by a neutron star merger preferentially only receiving axial ejecta

rather than disk ejecta? Or do Honda-like abundances (L-component) come from different sources (e.g. core-collapse supernovae with slightly neutron-rich conditions)? More investigation of the long-term mixing is necessary to understand the contribution of neutron star mergers to the different patterns found in the oldest observed stars. However, the dynamic and wind ejecta will not mix before they are substantially decelerated by the dilute ambient medium. For example, assuming a particle density of $\sim 1 \text{ cm}^{-3}$ for the ambient medium, the estimated deceleration time scale is of the order of several years. The dynamic ejecta expand earlier and with high initial velocities of $\sim 0.1c$. The neutrino-driven wind, in contrast, gets unbound after neutrinos have deposited enough energy. Therefore, the wind matter is ejected later and eventually reaches asymptotic velocities of up to $\sim 0.08c$. The different ejection times and velocities make it possible to observe a kilonova signal from different parts of the ejecta with different composition, as we discuss in the next section.

3.3. The electromagnetic signal: a semi-analytical model

The nucleosynthesis network allows us to compute radioactive heating rates for the wind outflow. Fig. 13 shows the heating rates for different bins, normalized to $\dot{\epsilon}_0(t) = 10^{10} t_d^{-1.3} \text{ erg g}^{-1} \text{ s}^{-1}$ with time t_d in units of days (Metzger et al. 2010; Korobkin et al. 2012). It is interesting to point out that all the normalized heating rates show considerable excess at $t \sim 4 \text{ h}$. This excess is caused by decay of radioactive nuclei in the vicinity of the first r-process abundance peak ($A \sim 80$), as those possess the highest mass fractions. The properties of the isotopes which contribute most to the heating rates in the neutrino-driven wind are listed in Tab. 1. On average, about 40% of the decay energy is carried away only by neutrinos. An additional fraction of energy is radiated away by escaping photons, while both the electrons and the remaining part of the photons thermalize. Therefore our hypothesis of an effective beta-decay thermalization fraction of 50% is reasonable.

TABLE 1
PROPERTIES OF THE DOMINANT β -DECAY NUCLEI AT $t \sim 1 \text{ DAY}$;
BASED ON THE DATA FROM NUDAT 2.6 DATABASE
(<http://www.nndc.bnl.gov/nudat2/>)

Isotope	$t_{1/2}$ (h)	Q ^(a) (MeV)	ϵ_e ^(b)	ϵ_ν ^(c)	ϵ_γ ^(d)	E_γ^{avg} ^(e) (MeV)
^{88}Kr	2.83	2.92	0.12	0.21	0.67	1.34
^{88}Rb	0.30	5.31	0.39	0.49	0.13	1.59
^{87}Kr	1.27	3.89	0.34	0.46	0.20	0.95
^{83}Br	2.37	0.98	0.33	0.66	0.007	0.46
^{81}Sr	0.37	3.93	0.28	0.37	0.35	0.42
^{78}Ge	1.47	0.96	0.24	0.47	0.29	0.28
^{78}As	1.51	4.21	0.30	0.39	0.31	0.94
^{77}Ge	11.2	2.70	0.23	0.36	0.41	0.47

(a) Total energy released in the decay; (b),(c),(d) Fraction of the decay energy released in electrons, neutrinos, and γ -rays; (e) Average photon energy produced in the decay.

Here we extend the semi-analytic model of Grossman et al. (2014) and Perego et al. (2014) to compute light curves. We assume that the wind shuts off immediately

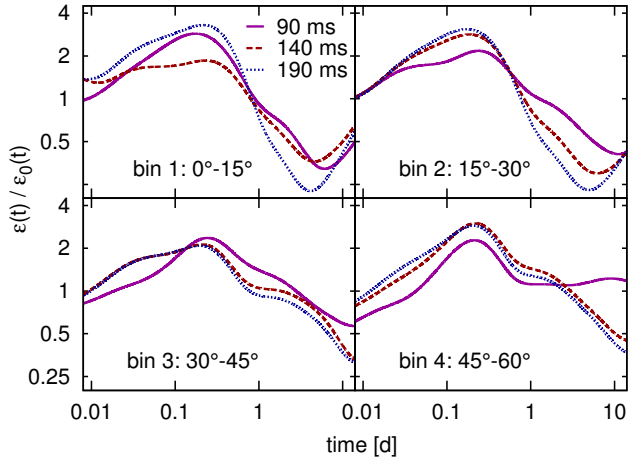


FIG. 13.— Radioactive heating rate, calculated with the nucleosynthesis network for a representative tracer of the neutrino-driven wind in each angular bin, normalized to the fitted expression $\dot{\epsilon}_0(t) = 10^{10} t_d^{-1.3} \text{ erg g}^{-1} \text{ s}^{-1}$ (see, e.g., Metzger et al. (2010); Kobrin et al. (2012)). In all cases the heating rate exhibits an excess by a factor of ~ 2.5 at $t \sim 4$ h.

after the collapse of the MNS and we explore collapse times of 90 ms, 140 ms and 190 ms after merger. The masses as well as average properties of the ejecta in the four bins for each of the cases are given in Tab. 2. The higher value of $\kappa = 10 \text{ cm}^2/\text{g}$ for the opacity in the last angular bin is justified by inspecting the distribution of mass fractions for heavy elements X_{heavy} (for mass numbers $A > 130$) in the neutrino-driven wind. This distribution is portrayed for extrapolated positions of the unbound tracers in Fig. 14 at $t = 50$ s after the merger. Mass fractions of heavy elements are marginal in the bins 1 – 3, but heap up in the area of bin 4. Reflecting that sizeable fractions of heavy elements are present, we adopt an opacity similar to the one of lanthanides or actinides (Kasen et al. 2013) for the last bin.

TABLE 2

PARAMETERS USED FOR COMPUTING LUMINOSITIES OF INDIVIDUAL BINS: SPANNED SOLID ANGLE, MASS OF THE BIN, AVERAGE ASYMPTOTIC VELOCITY OF THE EJECTA IN THE BIN, AND THE ADOPTED VALUE OF THE GRAY OPACITY.

t_{sim}	bin	$\Delta\Omega$	$\Delta m_{\text{ej}}/10^{-3} M_{\odot}$	v_{ej}/c	$\kappa [\text{cm}^2/\text{g}]$
90 ms	1	0.21409	0.013	0.05055	1
	2	0.62769	0.30	0.07974	1
	3	0.99851	0.77	0.07287	1
	4	1.30129	0.34	0.06808	10
140 ms	1	0.21409	0.05	0.04655	1
	2	0.62769	0.75	0.07483	1
	3	0.99851	1.99	0.07626	1
	4	1.30129	2.43	0.06694	10
190 ms	1	0.21409	0.07	0.04694	1
	2	0.62769	1.18	0.07325	1
	3	0.99851	3.39	0.07500	1
	4	1.30129	4.80	0.06466	10

Figure 15 illustrates our semianalytic model for light curve calculations, combining the results of this work and of Rosswog et al. (2014). The neutrino-driven wind is schematically shown in blue, while the gray-shaded areas tag the density of the dynamic ejecta in steps of 0.5 dex.

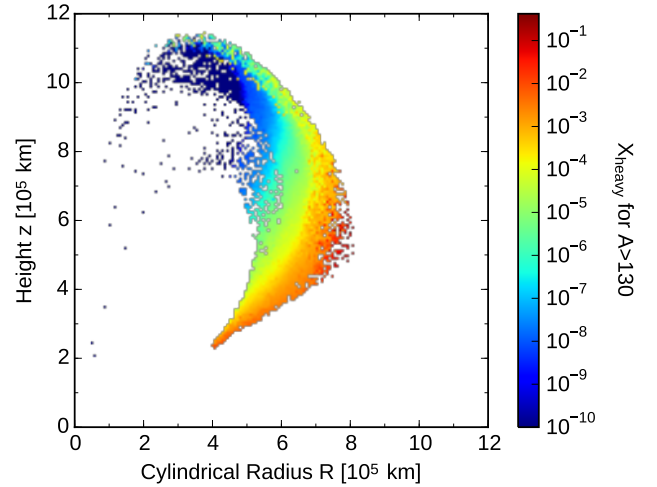


FIG. 14.— Distribution of summed up mass fractions for nuclei with mass number $A > 130$ in the neutrino-driven wind. The upper half space is shown in cylindrical coordinates for a time of 50 s after the merger. Tracers with vanishing total mass fractions $X_{\text{heavy}} < 10^{-10}$ are set to 10^{-10} .

We subdivide the wind outflow into the same four bins as in Section 2.1 above. Each bin is then approximated by a conical slice of a spherically-symmetric outflow with radial density distribution averaged over the bin and expanding with averaged velocity (a similar approach is employed in Margalit & Piran (2015) in a context of radio flares). All radiation is assumed to escape from the photosphere for each bin. Vector \vec{n} is the unit normal to the photosphere, and an observer is pointed to by a unit vector \vec{q} . The sketch also illustrates possible obscuration effects from the dynamic, very opaque ejecta, which are concentrated in a puffed up toroid around the equatorial plane. It is apparent that when viewed from the equatorial plane, the wind emission is completely obscured, while from the pole it is possible to observe at least the first three bins.

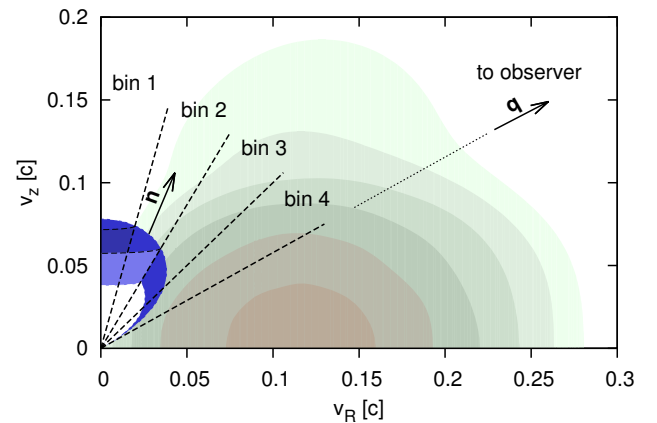


FIG. 15.— Morphology of the neutrino-driven wind (blue, this work) and dynamic ejecta (gray, cf. Rosswog et al. (2014)) in asymptotic velocity space, represented by a polar cut through the outflows. Shaded areas represent the density of dynamic ejecta, spaced by 0.5 dex from the maximum density at about $v_R \sim 0.115c$. Each angular bin is approximated by a conical slab with unit vector \vec{n} normal to the photosphere. An observer is pointed to by a unit vector \vec{q} .

For a bin k with mass Δm_k which spans solid angle $2\Delta\Omega_k$ (a factor of 2 takes into account upper and lower lobes), we take a spherically-symmetric outflow with mass $4\pi\Delta m_k/2\Delta\Omega_k$ and compute its isotropic bolometric luminosity $L_{k,\text{iso}}$ as described in Grossman et al. (2014) (see their Sect. 4.1).

The luminosity is generated by radioactive heating in the bulk of the outflow and the resulting photons escape from a photosphere. Spanning the same solid angle $2\Delta\Omega_k$ for each bin, the luminosity for bin k is a proportional fraction of isotropic luminosity of the spherical model:

$$L_k = \frac{\Delta\Omega_k}{2\pi} L_{k,\text{iso}}.$$

We then compute the total luminosity of the wind outflow by summing up individual bin contributions, ignoring possible radiative flux between the bins. Individual bin contributions for the combined bolometric luminosity of the neutrino-driven wind and dynamic ejecta for three cases of the MNS collapse time delay are displayed in Fig. 16. For the dynamic ejecta, we used an average case (model A from Grossman et al. (2014)) with mass $1.3 \cdot 10^{-2} M_\odot$. Notice that the luminosity of bin 1 is dimmer than for the bins 2 and 3, because it spans a smaller solid angle. The contribution from bin 4 is not only smaller, but also peaks much later (3–4 days) due to the high opacity caused by the very heavy nuclear content (Kasen et al. 2013), such that the medium becomes delayed transparent when the temperature has decreased.

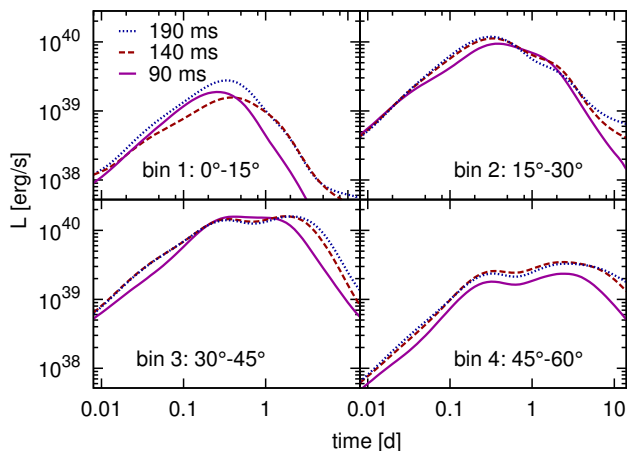


FIG. 16.— Individual contributions of the combined ejecta to the luminosity in the angular bins for three different MNS collapse times: 90 ms (solid), 140 ms (dashed) and 190 ms (dotted line).

Combined bolometric luminosities of the neutrino-driven wind and dynamic ejecta are shown in Fig. 17. A first peak of $L_{\text{peak}} \sim 4 \cdot 10^{40}$ erg/s is reached at about 4 h after the merger. This luminosity stays roughly constant for several days while rapidly shifting into the infrared band, as shown below. For higher MNS collapse times, the light curve exhibits a double peak structure, but overall the bolometric light curves on the plots exhibit no appreciable difference between different MNS collapse times.

Our simple model also allows to calculate approximate light curves in different bands for different orientations

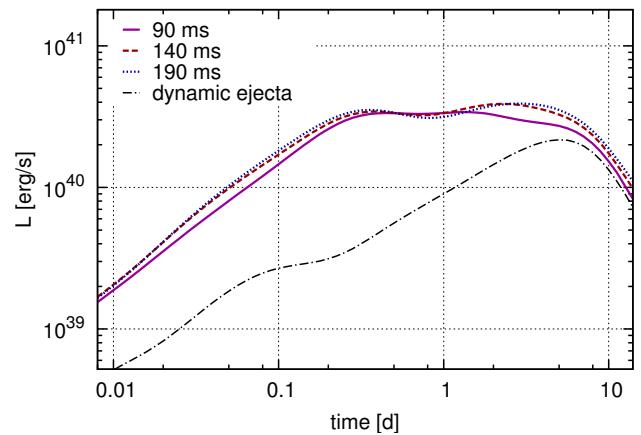


FIG. 17.— Bolometric luminosities for three cases of MNS collapse times: 90 ms (solid), 140 ms (dashed) and 190 ms (dotted line), computed by summing up contributions from individual bins and adding the contribution from dynamic ejecta. Contribution from the latter is also plotted separately (dash-dotted line).

of the system with respect to an observer. At any given moment t we can compute an effective temperature $T_{k,\text{eff}}$ for a bin k using the formula:

$$L_{k,\text{iso}}(t) = 4\pi r_{k,\text{ph}}^2 \cdot (\sigma_{\text{SB}} T_{k,\text{eff}}^4) \quad (3)$$

where $r_{k,\text{ph}}(t)$ is the photospheric radius for the spherical model of bin k , and σ_{SB} is the Stefan-Boltzmann constant. We make an assumption that all the flux is emitted from the photosphere with blackbody spectrum $B_\nu(T_{k,\text{eff}})$ and isotropic intensity (following Lambert's law). Then, the spectral flux in the direction \vec{q} is given by:

$$\mathcal{F}_\nu(\vec{q}, t) = \sum_k B_\nu(T_{k,\text{eff}}(t)) \iint_{(\vec{n}_k \cdot \vec{q}) > 0} (\vec{q} \cdot d\vec{\Omega}), \quad (4)$$

where \vec{n}_k is unit normal to the photosphere of bin k , and integration for each bin spans the part of the surface facing the observer (stated by the condition $(\vec{n}_k \cdot \vec{q}) > 0$). This is also illustrated in Fig. 15. Essentially, the integrals in this formula are simply time-independent geometric projections of the photosphere for each bin onto the viewing plane. They can be computed beforehand and used as weighting factors $p_k(\vec{q})$ for calculating the combined light curve:

$$\mathcal{F}_\nu(\vec{q}, t) = \sum_k p_k(\vec{q}) B_\nu(T_{k,\text{eff}}(t)). \quad (5)$$

After integrating $\mathcal{F}_\nu(\vec{q}, t)$ over certain frequency ranges, we obtain broadband light curves, shown in Fig. 18. The left-hand panel shows synthetic light curves for wind outflow only, while the right-hand panel displays the combined contribution from both wind and dynamic ejecta.

Orientation effects are displayed as a range of values for each band, with the maximum magnitude achieved when the system is viewed "face-on", i.e. from the pole. As pointed out by Kasen et al. (2015), even a small amount of dynamic ejecta can completely obscure the optical emission from the winds. Therefore, when adding up contributions from different bins and dynamic ejecta, we emulate this obscuration by excluding certain bins, depending on the inclination angle θ with respect to the

observer. Our choice of which bins to exclude is motivated by the geometry of the ejecta (depicted schematically in Fig. 15). Specifically, we assume that bin 4 is completely obscured for all observing angles; bins 2 and 3 are obscured when $\theta \geq 60^\circ$, and for the edge-on view with $\theta = 90^\circ$ the wind outflow emission is obscured completely. For this reason, depending on system orientation, the luminosity in different bands can vary by up to an order of magnitude, from bright blue when observed from the pole, to dim infrared when observed from the side.

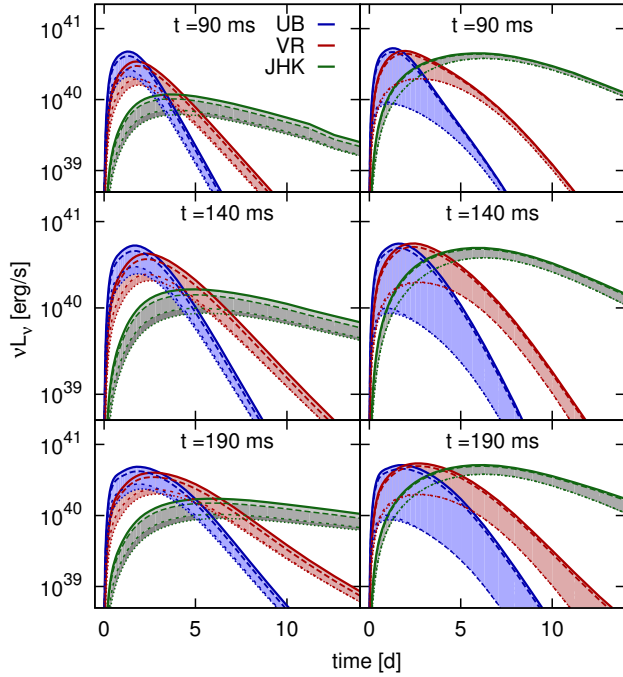


FIG. 18.— Broadband light curves of the wind outflow (left panel) and wind+dynamic ejecta (right panel), showing the combined blue (U+V bands), red (V+R) and infrared (J+H+K) contributions. The top, middle and bottom rows show the three cases of MNS collapse times: 90 ms, 140 ms and 190 ms, respectively. The range for each light curve spans possible inclination angles of the system axis with respect to the observer: 0° (solid) – view from the top, 30° (dashed), 60° (short dashes) and 90° (dotted) – view “edge-on”.

4. DISCUSSION AND CONCLUSIONS

We have presented a comprehensive study of the neutrino-driven wind nucleosynthesis in the aftermath of a double neutron star merger. We have focused on the initial phase where the remnant consists of a MNS surrounded by a massive accretion disk. The current nucleosynthesis study is based on the first three-dimensional simulation of such a wind (Perego et al. 2014), sampling the wind outflow by ~ 17000 tracer particles. For every tracer, nucleosynthesis calculations are performed in a post-processing step. This work advances the preliminary study in Perego et al. (2014) that only used 10 tracers and thus led to a slight overestimation of the amount of heavy elements ($A > 130$) produced, whereas the total mass ejected in the wind was underestimated. Our main results are summarized and discussed alongside their uncertainties in the following.

The *abundance distribution* in the neutrino-driven wind is characterized by the production of lighter heavy elements ($A \lesssim 130$). We have found a time and angle dependency of the composition correlated with the electron fraction evolution. Elements heavier than $A > 130$ are produced only at early times, in an almost negligible amount and in the wind region that is closest to the disk (between 45° and 60° from the pole, bin 4 in Fig. 7). In contrast, matter ejected more perpendicular to the disk (bin 1: $0^\circ - 15^\circ$) produces only nuclei up to the first r-process peak ($A < 100$). The nucleosynthesis path of the neutrino-driven wind after a neutron star merger does not reach the heaviest nuclei, in some cases it even stops before $N = 82$. Relevant nuclear physics input (e.g., nuclear masses and beta-decays) along the path is known or will be measured in current and future generation facilities in the coming years to provide more reliable data. Our calculations are based on the FRDM mass model (Möller et al. 1995) and consistently calculated nuclear reaction rates (Rauscher & Thielemann 2000). A detailed study of the impact of the nuclear physics input can give rise to new insights (de Jesús Mendoza-Temis et al. 2014; Eichler et al. 2015; Goriely et al. 2015). Especially near the shell closure at $N = 82$ nuclear masses and neutron captures may have an impact on the abundances before the second r-process peak where we find a significant trough.

The *electron fraction* is here the key parameter to understand the characteristics of abundances. It covers a broad range from 0.1 to 0.4 with average values of $Y_e \sim 0.33$. As noted already in earlier studies (see in particular Fig. 8 in Korobkin et al. (2012) where the Y_e -dependence was explored; Freiburghaus et al. 1999a; Kasen et al. 2015), $Y_e \approx 0.25$ is the threshold beyond which no more heavy r-process elements are formed. Since abundances depend strongly on Y_e , an accurate treatment of weak reactions is crucial and can be achieved by improving the neutrino transport and including more neutrino-matter reactions. We have estimated a $\sim 20\%$ error on the electron fraction due to the approximate transport scheme. This is suggested by the comparison of neutrino luminosities and mean energies from Perego et al. (2014) and Dessart et al. (2009), which are among the best treatments for these kinds of systems (see also Just et al. (2015a,b); Fernández & Metzger (2013)). For the neutrino-matter interactions, a small variation of Y_e can arise from a detailed inclusion of the (anti)neutrino absorption including weak magnetism and medium effects (Roberts et al. 2012; Martínez-Pinedo et al. 2012).

The *amount of ejecta* also depends on angle and time. As the wind is preferentially driven out at lower latitudes, bin 3 and 4 contain roughly 6 times the matter of bins 1 and 2. About 110 ms after the merger a steady-state is reached in terms of mass loss. The total unbound mass depends crucially on the time when the MNS collapses and if it survives for ~ 200 ms as much as $9 \cdot 10^{-3} M_\odot$ can become unbound (i.e. $\sim 5\%$ of the initial mass of the accretion disk). This amount of matter rivals the dynamic ejecta that are typically found to be of order of $0.01 M_\odot$ ($1.3 \cdot 10^{-2} M_\odot$ for the specific case considered here). Recent studies (Fernández & Metzger 2013; Kasen et al. 2015; Just et al. 2015a; Sekiguchi et al. 2015) indicate that the winds switches off rapidly once a black hole forms. Approximately half of the neutrino luminosity is

provided by the MNS. Therefore, when the black hole forms this contribution vanishes and the disk structure may significantly change. It is possible that general relativistic effects also have a non-negligible impact on the disk winds from a MNS and accretion disk system, as is the case for neutron star - black hole systems (Caballero et al. 2015).

The angle dependency of the composition may have consequences for the *mixing* with other ejecta. Both dynamic and viscous ejecta contribute also to the production of heavy r-process elements beyond the second peak ($A > 130$). If wind material perfectly mixes with these ejection channels, its contribution may lead to variations for the lighter heavy elements (i.e., $A < 130$). This variation is indeed observed in stars with high enrichment of heavy r-process elements. However, if the mixing is not perfect one could speculate that neutron star mergers with long-lived MNS may produce different abundance patterns including one with low enrichment of heavy r-process elements. This kind of pattern (“Honda-like pattern”, see Honda et al. (2004, 2007)) is observed in a few very old stars and its origin is still unknown. However, detailed mixing models following the late evolution of the three nucleosynthesis-relevant ejecta are required before concluding about the contribution of neutron star mergers to observed abundance patterns.

The initial separation of wind and dynamic ejecta allows to describe the individual contributions to the *light curve* of the electromagnetic transient. We use a semi-analytic radiation transport model to calculate the luminosities of the wind and dynamic ejecta. The light curve of the wind ejecta peaks after ~ 4 hours in the blue compared to the one of the dynamic ejecta that peaks few days after the merger in the infrared. The combined light curve will significantly depend on the observing angle, as previously pointed out by Kasen et al. (2015). Due to the high line expansion opacities of lanthanides and actinides (Kasen et al. 2013), even small amounts of dynamic ejecta along the line of sight can completely obscure the blue transient from the wind. Since the morphology of dynamic ejecta is such that it leaves polar regions evacuated, it is far more likely to detect the blue component when the system is observed from the pole. In Fig. 18, we have presented the light curves of obscured and unobscured winds as a function of angle and time of black hole formation. The luminosity in the blue band exhibits a much higher dependency on the viewing angle compared to the luminosity in the infrared, in agreement with previous studies (Kasen et al. 2015). This significant anisotropy needs to be taken into account when assessing detectability of optical counterparts to neutron star mergers. Another interesting feature is the noticeable dependence of the position of optical peaks on the time of black hole formation (apparent in Fig. 18). A longer collapse time leads to a later and more prolonged peak in both U+B and V+R bands, while this trend is washed out in the infrared. Although at this point it is difficult to draw any quantitative conclusions due to limitations of our model, our results suggest a possibility

to use the position and duration of optical transients as proxies for the time of black hole formation (see also Metzger & Fernández (2014)). More work is needed to take into account additional channels of late-time ejecta production, and to improve radiation treatment (see, e.g., Kasen et al. (2015)).

Our results clearly indicate the importance of neutrino-driven winds for the nucleosynthesis of neutron star mergers. It needs to be stated, however, that these results have been obtained based on Newtonian hydrodynamics simulations and that general-relativistic effects could potentially modify some of our conclusions. For example, recent studies in full GR (Hotokezaka et al. 2011, 2013; Sekiguchi et al. 2015) and in the conformal flatness approximation (Bauswein et al. 2013) agree that shocks are more important for the dynamic ejecta in the GR case, especially when a soft equation of state is used. This is mainly because the stars are – for a given EOS – more compact due to the stronger relativistic gravity and hence lead to larger velocities prior to contact. A softer EOS leads compared to a stiff one to more compact stars and also to smaller sound speeds which, in turn, make the occurrence of shocks more likely. Therefore, the dynamic ejecta are dominated by the hotter “interaction component” while Newtonian ejecta are dominated by the colder, unshocked “tidal component” (Korobkin et al. 2012)³. Therefore, a GR calculation will plausibly cause a higher temperature environment which is expected to lead to larger electron fractions in the ejecta. Due to shock-heating it is also likelier that unbound material is ejected out-of-plane. Thus a neutron star merger could actually, consistent with our findings here, produce a very broad range of r-process abundances (Wanajo et al. 2014; Just et al. 2015a).

Understanding the interplay of all ejecta from neutron star mergers is key to decode the diverse aspects of this astrophysical site. Further detailed simulations and complete nucleosynthesis studies will help to pin down the role of neutron star mergers for the origin of the heavy elements in the universe as well as to predict reliable electromagnetic counterparts for the detection of GWs.

AA, AP, and DM are supported by the Helmholtz-University Young Investigator grant No. VH-NG-825. AP acknowledges the use of computational resources provided by the Swiss Super Computing Center (CSCS), under the allocation grant s414. FKT is supported by the Schweizerische Nationalfond (SNF) and the ERC Advanced Grant FISH. OK and SR were supported by Deutsche Forschungsgemeinschaft (DFG) under grant number RO-3399/5-1 and by the Swedish Research Council (VR) under grant 621-2012-4870. Some of the simulations have been obtained on the facilities of the The North-German Supercomputing Alliance (HLRN). The authors thank also “NewCompStar”, COST Action MP1304, for support. We also thank the Institute for Nuclear Theory where discussions and contributions to this work were made during the program “INT-14-2b” about nucleosynthesis and chemical evolution.

³ Despite these differences, the overall amount of dynamic ejecta is in good agreement between different studies. There is a dependence on the mass ratio and the equation of state, with softer EOSs ejecting more mass in GR calculations, but ejecta masses up to a few percent of the solar mass can be reached, see, e.g. Tab. 1 in

REFERENCES

- Arcones, A., Janka, H.-T., & Scheck, L. 2007, *A&A*, 467, 1227
- Arcones, A. & Montes, F. 2011, *ApJ*, 731, 5
- Arcones, A. & Thielemann, F.-K. 2013, *Journal of Physics G Nuclear Physics*, 40, 013201
- Argast, D., Samland, M., Thielemann, F.-K., & Qian, Y.-Z. 2004, *A&A*, 416, 997
- Barnes, J. & Kasen, D. 2013, *ApJ*, 775, 18
- Bauswein, A., Goriely, S., & Janka, H.-T. 2013, *ApJ*, 773, 78
- Beloborodov, A. M. 2008, in *American Institute of Physics Conference Series*, Vol. 1054, American Institute of Physics Conference Series, ed. M. Axelsson, 51–70
- Berger, E., Fong, W., & Chornock, R. 2013, *ApJ*, 774, L23
- Caballero, O. L., Surman, R., & McLaughlin, G. C. 2015, 93, 3002
- Cescutti, G., Romano, D., Matteucci, F., Chiappini, C., & Hirschi, R. 2015, *A&A*, 577, A139
- de Jesús Mendoza-Temis, J., Martínez-Pinedo, G., Langanke, K., Bauswein, A., & Janka, H.-T. 2014, *ArXiv e-prints*
- Dessart, L., Ott, C. D., Burrows, A., Rosswog, S., & Livne, E. 2009, *ApJ*, 690, 1681
- Eichler, D., Livio, M., Piran, T., & Schramm, D. N. 1989, *Nature*, 340, 126
- Eichler, M., Arcones, A., Kelic, A., Korobkin, O., Langanke, K., Marketin, T., Martínez-Pinedo, G., Panov, I. V., Rauscher, T., Rosswog, S., Winteler, C., Zinner, N. T., & Thielemann, F.-K. 2015, *The Astrophysical Journal*, 808, 30
- Fernández, R. & Metzger, B. D. 2013, *MNRAS*, 435, 502
- Fernández, R., Quataert, E., Schwab, J., Kasen, D., & Rosswog, S. 2015, *MNRAS*, 449, 390
- Fischer, T., Whitehouse, S. C., Mezzacappa, A., Thielemann, F.-K., & Liebendörfer, M. 2010, *A & A*, 517, A80
- Foucart, F., O'Connor, E., Roberts, L., Duez, M. D., Haas, R., Kidder, L. E., Ott, C. D., Pfeiffer, H. P., Scheel, M. A., & Szilagyi, B. 2015, *Phys. Rev. D*, 91, 124021
- Freiburghaus, C., Rembges, J.-F., Rauscher, T., Kolbe, E., Thielemann, F.-K., Kratz, K.-L., Pfeiffer, B., & Cowan, J. J. 1999a, *ApJ*, 516, 381
- Freiburghaus, C., Rosswog, S., & Thielemann, F.-K. 1999b, *ApJ*, 525, L121
- Fröhlich, C., Martínez-Pinedo, G., Liebendörfer, M., Thielemann, F.-K., Bravo, E., Hix, W. R., Langanke, K., & Zinner, N. T. 2006, *Phys. Rev. Lett.*, 96, 142502
- Fujimoto, S.-i., Kotake, K., Yamada, S., Hashimoto, M.-a., & Sato, K. 2006, *ApJ*, 644, 1040
- Fujimoto, S.-I., Nishimura, N., & Hashimoto, M.-A. 2008, *ApJ*, 680, 1350
- Goriely, S. 2015, *European Physical Journal A*, 51, 22
- Goriely, S., Bauswein, A., & Janka, H.-T. 2011, *ApJ*, 738, L32
- Goriely, S., Bauswein, A., Just, O., Pllumbi, E., & Janka, H.-T. 2015, *MNRAS*, 452, 3894
- Goriely, S., Sida, J.-L., Lemaître, J.-F., Panebianco, S., Dubray, N., Hilaire, S., Bauswein, A., & Janka, H.-T. 2013, *Physical Review Letters*, 111, 242502
- Grossman, D., Korobkin, O., Rosswog, S., & Piran, T. 2014, *MNRAS*, 439, 757
- Hansen, C. J., Montes, F., & Arcones, A. 2014, *ApJ*, 797, 123
- Hempel, M., Fischer, T., Schaffner-Bielich, J., & Liebendörfer, M. 2012, *ApJ*, 748, 70
- Hoffman, R. D., Woosley, S. E., & Qian, Y.-Z. 1997, *ApJ*, 482, 951
- Honda, S., Aoki, W., Ishimaru, Y., & Wanajo, S. 2007, *ApJ*, 666, 1189
- Honda, S., Aoki, W., Ishimaru, Y., Wanajo, S., & Ryan, S. G. 2006, *ApJ*, 643, 1180
- Honda, S., Aoki, W., Kajino, T., Ando, H., Beers, T. C., Izumiura, H., Sadakane, K., & Takada-Hidai, M. 2004, *ApJ*, 607, 474
- Hotkezaka, K., Kiuchi, K., Kyutoku, K., Muranushi, T., Sekiguchi, Y.-i., Shibata, M., & Taniguchi, K. 2013, *Phys. Rev. D*, 88, 044026
- Hotkezaka, K., Kyutoku, K., Okawa, H., Shibata, M., & Kiuchi, K. 2011, *Phys. Rev. D*, 83, 124008
- Hüdepohl, L., Müller, B., Janka, H.-T., Marek, A., & Raffelt, G. G. 2010, *Physical Review Letters*, 104, 251101
- Just, O., Bauswein, A., Pulpillo, R. A., Goriely, S., & Janka, H.-T. 2015a, *MNRAS*, 448, 541
- Just, O., Obergaulinger, M., & Janka, H.-T. 2015b, *ArXiv e-prints*
- Käppeli, R., Whitehouse, S. C., Scheidegger, S., Pen, U.-L., & Liebendörfer, M. 2011, *ApJS*, 195, 20
- Kasen, D., Badnell, N. R., & Barnes, J. 2013, *ApJ*, 774, 25
- Kasen, D., Fernández, R., & Metzger, B. D. 2015, *MNRAS*, 450, 1777
- Korobkin, O., Rosswog, S., Arcones, A., & Winteler, C. 2012, *MNRAS*, 426, 1940
- Kulkarni, S. R. 2005, *ArXiv Astrophysics e-prints*
- Lattimer, J. M. & Schramm, D. N. 1974, *ApJ*, 192, L145
- . 1976, *ApJ*, 210, 549
- Lee, W. H., Ramirez-Ruiz, E., & López-Cámara, D. 2009, *ApJL*, 699, L93
- Li, L.-X. & Paczyński, B. 1998, *ApJ*, 507, L59
- Lodders, K. 2003, *ApJ*, 591, 1220
- Margalit, B. & Piran, T. 2015, *MNRAS*, 452, 3419
- Martínez-Pinedo, G., Fischer, T., Lohs, A., & Huther, L. 2012, *Physical Review Letters*, 109, 251104
- Matteucci, F., Romano, D., Arcones, A., Korobkin, O., & Rosswog, S. 2014, *MNRAS*, 438, 2177
- Metzger, B. D. & Berger, E. 2012, *ApJ*, 746, 48
- Metzger, B. D. & Fernández, R. 2014, *MNRAS*, 441, 3444
- Metzger, B. D., Martínez-Pinedo, G., Darbha, S., Quataert, E., Arcones, A., Kasen, D., Thomas, R., Nugent, P., Panov, I. V., & Zinner, N. T. 2010, *MNRAS*, 406, 2650
- Metzger, B. D., Piro, A. L., & Quataert, E. 2008, *MNRAS*, 390, 781
- Möller, P., Nix, J. R., Myers, W. D., & Swiatecki, W. J. 1995, *At. Data Nucl. Data Tables*, 59, 185
- Möller, P., Pfeiffer, B., & Kratz, K.-L. 2003, *Phys. Rev. C*, 67, 055802
- Mösta, P., Richers, S., Ott, C. D., Haas, R., Piro, A. L., Boydstun, K., Abdikamalov, E., Reisswig, C., & Schnetter, E. 2014, *ApJ*, 785, L29
- Murguía-Berthier, A., Montes, G., Ramirez-Ruiz, E., De Colle, F., & Lee, W. H. 2014, *ApJL*, 788, L8
- Neilsen, D., Liebbling, S. L., Anderson, M., Lehner, L., O'Connor, E., & Palenzuela, C. 2014, *Phys. Rev. D*, 89, 104029
- Nishimura, N., Takiwaki, T., & Thielemann, F.-K. 2015, *ApJ*, 810, 109
- Nissanke, S., Kasliwal, M., & Georgieva, A. 2013, *ApJ*, 767, 124
- Oechslin, R., Janka, H., & Marek, A. 2007, *A & A*, 467, 395
- Panov, I. V., Kolbe, E., Pfeiffer, B., Rauscher, T., Kratz, K.-L., & Thielemann, F.-K. 2005, *Nucl. Phys. A*, 747, 633
- Panov, I. V., Korneev, I. Y., Rauscher, T., Martínez-Pinedo, G., Kelić-Heil, A., Zinner, N. T., & Thielemann, F.-K. 2010, *A&A*, 513, A61
- Panov, I. V., Korneev, I. Y., & Thielemann, F.-K. 2008, *Astronomy Letters*, 34, 189
- Perego, A., Rosswog, S., Cabezón, R. M., Korobkin, O., Käppeli, R., Arcones, A., & Liebendörfer, M. 2014, *MNRAS*, 443, 3134
- Petermann, I., Langanke, K., Martínez-Pinedo, G., Panov, I. V., Reinhard, P.-G., & Thielemann, F.-K. 2012, *European Physical Journal A*, 48, 122
- Piran, T., Nakar, E., & Rosswog, S. 2013, *MNRAS*, 430, 2121
- Price, D. J. & Rosswog, S. 2006, *Science*, 312, 719
- Qian, Y.-Z. & Wasserburg, G. J. 2007, *Phys. Rep.*, 442, 237
- Qian, Y.-Z. & Woosley, S. E. 1996, *ApJ*, 471, 331
- Rauscher, T. & Thielemann, F.-K. 2000, *At. Data Nucl. Data Tables*, 75, 1
- Roberts, L. F., Kasen, D., Lee, W. H., & Ramirez-Ruiz, E. 2011, *ApJL*, 736, L21
- Roberts, L. F., Reddy, S., & Shen, G. 2012, *Phys. Rev. C*, 86, 065803
- Roberts, L. F., Woosley, S. E., & Hoffman, R. D. 2010, *ApJ*, 722, 954
- Roederer, I. U., Cowan, J. J., Karakas, A. I., Kratz, K.-L., Lugaro, M., Simmerer, J., Farouqi, K., & Sneden, C. 2010, *ApJ*, 724, 975

Rosswog (2015) for a compilation of the ejecta mass results from different groups. It can, however, not be excluded that also purely numerical effects still impact on the results.

- Rosswog, S. 2013, Royal Society of London Philosophical Transactions Series A, 371, 20272
- . 2015, International Journal of Modern Physics D, 24, 30012
- Rosswog, S., Korobkin, O., Arcones, A., Thielemann, F.-K., & Piran, T. 2014, MNRAS, 439, 744
- Rosswog, S., Liebendörfer, M., Thielemann, F.-K., Davies, M., Benz, W., & Piran, T. 1999, A & A, 341, 499
- Rosswog, S. & Ramirez-Ruiz, E. 2002, MNRAS, 336, L7
- Ruffert, M., Janka, H., Takahashi, K., & Schaefer, G. 1997, A & A, 319, 122
- Sekiguchi, Y., Kiuchi, K., Kyutoku, K., & Shibata, M. 2015, Phys. Rev. D, 91, 064059
- Shen, S., Cooke, R. J., Ramirez-Ruiz, E., Madau, P., Mayer, L., & Guedes, J. 2015, ApJ, 807, 115
- Snedden, C., Cowan, J. J., & Gallino, R. 2008, ARA&A, 46, 241
- Snedden, C., Cowan, J. J., Lawler, J. E., Ivans, I. I., Burles, S., Beers, T. C., Primas, F., Hill, V., Truran, J. W., Fuller, G. M., Pfeiffer, B., & Kratz, K.-L. 2003, ApJ, 591, 936
- Tanaka, M. & Hotokezaka, K. 2013, ApJ, 775, 113
- Tanvir, N. R., Levan, A. J., Fruchter, A. S., Hjorth, J., Hounsell, R. A., Wiersema, K., & Tunnicliffe, R. L. 2013, Nature, 500, 547
- Timmer, F. X. & Swesty, F. D. 2000, ApJS, 126, 501
- van de Voort, F., Quataert, E., Hopkins, P. F., Keres, D., & Faucher-Giguere, C.-A. 2015, MNRAS, 447, 140
- Wallerstein, G., Greenstein, J. L., Parker, R., Helfer, H. L., & Aller, L. H. 1963, ApJ, 137, 280
- Wanajo, S., Sekiguchi, Y., Nishimura, N., Kiuchi, K., Kyutoku, K., & Shibata, M. 2014, ApJ, 789, L39
- Wehmeyer, B., Pignatari, M., & Thielemann, F.-K. 2015, MNRAS, 452, 1970
- Winteler, C. 2012, PhD thesis, University Basel, CH
- Winteler, C., Käppeli, R., Perego, A., Arcones, A., Vassetz, N., Nishimura, N., Liebendörfer, M., & Thielemann, F.-K. 2012, ApJ, 750, L22
- Yang, B., Jin, Z.-P., Li, X., Covino, S., Zheng, X.-Z., Hotokezaka, K., Fan, Y.-Z., Piran, T., & Wei, D.-M. 2015, Nature Communications, 6, 7323